Astronomy & Astrophysics

Eyes on K2-3: A system of three likely sub-Neptunes characterized with HARPS-N and HARPS[*]

M. Damasso[1], A. S. Bonomo[1], N. Astudillo-Defru[2], X. Bonfils[3], L. Malavolta[4,5], A. Sozzetti[1], E. Lopez[6], L. Zeng[7],
R. D. Haywood[8], J. M. Irwin[8], A. Mortier[9], A. Vanderburg[8,10,**], J. Maldonado[11], A. F. Lanza[12], L. Affer[11],
J.-M. Almenara[2], S. Benatti[5], K. Biazzo[12], A. Bignamini[13], F. Borsa[14], F. Bouchy[2], L. A. Buchhave[15],
A. C. Cameron[9], I. Carleo[5], D. Charbonneau[8], R. Claudi[5], R. Cosentino[16], E. Covino[17], X. Delfosse[3], S. Desidera[5],
L. Di Fabrizio[16], C. Dressing[18], M. Esposito[17], R. Fares[12], P. Figueira[19,20], A. F. M. Fiorenzano[16], T. Forveille[3],
P. Giacobbe[1], E. González-Álvarez[11], R. Gratton[5], A. Harutyunyan[16], J. Asher Johnson[8], D. W. Latham[8], G. Leto[12],
M. Lopez-Morales[8], C. Lovis[2], A. Maggio[11], L. Mancini[1,21,22], S. Masiero[11], M. Mayor[2], G. Micela[11],
E. Molinari[16,23], F. Motalebi[2], F. Murgas[24,25], V. Nascimbeni[4,5], I. Pagano[12], F. Pepe[2], D. F. Phillips[8], G. Piotto[4,5],
E. Poretti[14], M. Rainer[14], K. Rice[26], N. C. Santos[20,27], D. Sasselov[8], G. Scandariato[12], D. Ségransan[2], R. Smareglia[13],
S. Udry[2], C. Watson[28], and A. Wünsche[3]

(Affiliations can be found after the references)

ABSTRACT

Context. M-dwarf stars are promising targets for identifying and characterizing potentially habitable planets. K2-3 is a nearby (45 pc), early-type M dwarf hosting three small transiting planets, the outermost of which orbits close to the inner edge of the stellar (optimistic) habitable zone. The K2-3 system is well suited for follow-up characterization studies aimed at determining accurate masses and bulk densities of the three planets.

Aims. Using a total of 329 radial velocity measurements collected over 2.5 years with the HARPS-N and HARPS spectrographs and a proper treatment of the stellar activity signal, we aim to improve measurements of the masses and bulk densities of the K2-3 planets. We use our results to investigate the physical structure of the planets.

Methods. We analysed radial velocity time series extracted with two independent pipelines using Gaussian process regression. We adopted a quasi-periodic kernel to model the stellar magnetic activity jointly with the planetary signals. We used Monte Carlo simulations to investigate the robustness of our mass measurements of K2-3 c and K2-3 d, and to explore how additional high-cadence radial velocity observations might improve these values.

Results. Even though the stellar activity component is the strongest signal present in the radial velocity time series, we are able to derive masses for both planet b ($M_b = 6.6 \pm 1.1\ M_\oplus$) and planet c ($M_c = 3.1^{+1.3}_{-1.2}\ M_\oplus$). The Doppler signal from K2-3 d remains undetected, likely because of its low amplitude compared to the radial velocity signal induced by the stellar activity. The closeness of the orbital period of K2-3 d to the stellar rotation period could also make the detection of the planetary signal complicated. Based on our ability to recover injected signals in simulated data, we tentatively estimate the mass of K2-3 d to be $M_d = 2.7^{+1.2}_{-0.8}\ M_\oplus$. These mass measurements imply that the bulk densities and therefore the interior structures of the three planets may be similar. In particular, the planets may either have small H/He envelopes (<1%) or massive water layers, with a water content ≥50% of their total mass, on top of rocky cores. Placing further constraints on the bulk densities of K2-3 c and d is difficult; in particular, we would not have been able to detect the Doppler signal of K2-3 d even by adopting a semester of intense, high-cadence radial velocity observations with HARPS-N and HARPS.

Key words. stars: individual: K2-3 – planets and satellites: detection – planets and satellites: composition – techniques: radial velocities – stars: individual: EPIC 201367065 – stars: individual: 2MASS 11292037-0127173

1. Introduction

In the last decade, the search for potentially habitable exoplanets has focussed particularly on M-dwarf stars. In this context, we regard a potentially habitable exoplanet as, in the broadest sense, one that orbits within or close to the habitable zone (HZ) of the parent star. Using the two main indirect detection methods,

photometric transits and radial velocity (RV), potentially habitable exoplanets can be detected more easily around M dwarfs than around earlier type stars.

However, even M dwarfs present some challenges because of their faintness, their magnetic activity, and the difficulty in measuring accurate stellar parameters, which are essential if we wish to accurately determine the planetary parameters. Several exoplanet surveys have been devised to target M dwarfs specifically, such as the current ground-based photometric experiments MEarth (Irwin et al. 2015), APACHE (Sozzetti et al. 2013), and TRAPPIST (Gillon et al. 2017); the upcoming

---

SPECULOOS[1] and ExTrA (Bonfils et al. 2015) projects; and surveys exploiting high-resolution and high-stability spectrographs (e.g. Bonfils et al. 2013; Delfosse et al. 2013b; Affer et al. 2016 and the HADES paper series; Quirrenbach et al. 2016).

Results from the *Kepler* and K2 missions have also been used to provide estimates for the occurrence of planets in the HZ of M dwarfs (e.g. Dressing & Charbonneau 2013, 2015; Howell et al. 2014; Dressing et al. 2017a, b). These analyses suggest that small, low-mass planets are abundant around M dwarfs, and a significant percentage of these planets may have properties suitable for the emergence of life (Dressing & Charbonneau 2015; Tuomi et al. 2014). Space-based missions planned for the very near future, such as TESS (Ricker et al. 2014), CHEOPS (Fortier et al. 2014), and PLATO (Rauer et al. 2014) will target bright and nearby M dwarfs to detect potentially habitable planets, while JWST (Beichman et al. 2014) and ground-based 25–40 m class telescopes will characterize the atmospheres of these planets.

Some of the most intriguing exoplanet discoveries of the last few years are temperate planets around nearby M dwarfs, which orbit close to, or within, the predicted circumstellar HZ. For example, temperate, low-mass planets have been discovered around a number of nearby M-dwarf stars including Proxima Centauri (Anglada-Escudé et al. 2016), TRAPPIST-1 (Gillon et al. 2017), LHS 1140 (Dittmann et al. 2017), GJ 273 (Astudillo-Defru et al. 2017), K2-18 (Cloutier et al. 2017), GJ 667 C (Anglada-Escudé et al. 2013; Delfosse et al. 2013a; Feroz & Hobson 2014), and Ross 128 (Bonfils et al. 2018). These new discoveries have stimulated many theoretical studies addressing the habitability of planets orbiting M dwarfs (see e.g. Shields et al. 2016 for a review on this topic). Open questions regarding the true habitability of these temperate planets include the influence of the spectral energy distribution and the activity of M dwarfs on planetary atmospheres, as well as the effect of tidal locking. Potentially habitable planets around M dwarfs are likely subject to physical conditions that are very different from those experienced on Earth, and their properties may also depend strongly on the M-dwarf spectral subtype.

Indeed, M dwarfs that host temperate rocky planets exhibit a wide range of physical properties that might influence habitability. GJ 273, Ross 128, LHS 1140, Proxima Centauri, and TRAPPIST-1 are mid- to late-M dwarfs (M3.5V, M4V, M4.5V, M5.5V, and M8V, respectively). GJ 273 and Ross 128 have weak magnetic activity, while Proxima Centauri and TRAPPIST-1 have high activity levels, which probably has a large impact on the potential habitability of their planets. K2-18 is, instead, an earlier type M2.5 dwarf with low chromospheric activity, and GJ 667 C is a quiet M1.5 dwarf. The fact that these temperate planets are located at different distances from host stars spanning different spectral subtypes makes their comparative characterization particularly interesting. Unfortunately, many of these planets either do not transit or their parent star is too faint to permit detailed follow-up, making it difficult to robustly characterize these planets and hence study their interior structures and compositions.

Within this context, the planetary system around K2-3 (EPIC 201367065), a nearby (45 pc) M0 dwarf (V = 12 mag; J = 9.4 mag), presents an interesting opportunity for follow-up studies. Observations from the K2 mission revealed that K2-3 hosts at least three transiting small planets (Crossfield

et al. 2015): K2-3 b ($R_p = 2\,R_\oplus$, P_{orb} = 10 days), K2-3 c ($R_p = 1.7\,R_\oplus$, P_{orb} = 24.6 days), and K2-3 d ($R_p = 1.6\,R_\oplus$, P_{orb} = 45.5 days). According to the optimistic HZ boundaries derived by Kopparapu et al. (2013, 2014), planet K2-3 d orbits close to the inner edge of the HZ of its host star. A particularly intriguing property of the K2-3 system is that the host star is bright enough to estimate the masses of these planets using existing high-resolution stabilized spectrographs.

Measuring the masses of the K2-3 planets would be interesting for several reasons. First, by determining the mass and bulk density of the temperate planet K2-3d, we can extend the study of planets orbiting close or within the HZ to earlier type host stars than those discussed earlier. Moreover, because of their measured sizes, planets K2-3 c and K2-3 d are optimal targets to test the results of Rogers (2015), who found that the majority of the observed planets with radius $R_p \geq 1.6\,R_\oplus$ have densities too low to have a bulk rocky composition. Fulton et al. (2017) cast light on this result by finding evidence for a bimodal distribution of small planet sizes orbiting stars with $T_{eff} > 4500$ K with periods less than 100 days. Planets are preferentially found with radii around $\sim 1.3\,R_\oplus$ and $\sim 2.4\,R_\oplus$, with a region between 1.5 and 2.0 $R_\oplus$ where planet occurrence is rare. This bi-modality likely reflects a separation between purely rocky planets and rocky cores surrounded by varying amounts of lower density volatile material. K2-3 c and K2-3 d fall within the gap between the two peaks in the planet radius distribution and orbit a star cooler than 4000 K, making them interesting test cases for understanding the composition of planets in this size regime at lower stellar irradiation than most of the planets analysed by Fulton et al. (2017).

Previously, other groups have recognized the appeal of the K2-3 system and have begun conducting RV follow-ups (Almenara et al. 2015; Dai et al. 2016). Almenara et al. (2015) found that stellar activity has a major impact on RV observations of K2-3 and, based on their single semester of monitoring, were unable to measure the masses of K2-3 c and K2-3 d robustly. Accurate determination of the masses of K2-3 c and K2-3 d evidently requires a larger dataset and denser sampling to trace out the activity signal.

We present the results of an intense RV follow-up of K2-3 conducted over three seasons with the HARPS-N and HARPS spectrographs. Despite having data from several independent teams, and having precise transit ephemeris from high-precision photometry (Beichman et al. 2016; Fukui et al. 2016), measuring the mass of K2-3 c and K2-3 d has been challenging.

The paper is organized as follows. We first introduce the RV datasets and discuss the significant signals present in the data through a frequency analysis (Sect. 2). In Sect. 3 we present updated stellar parameters and analyse the photometric light curves of K2-3 and the Hα line activity indicator time series. The analysis of the RVs with Gaussian processes (GP) is described in Sect. 4. The significance of our best-fit solution for the masses of K2-3 c and K2-3 d is investigated through Monte Carlo simulations and is discussed in Sect. 5. Finally, we present the mass-radius diagram for the K2-3 planets and discuss the implications of our findings for their bulk composition.

2. Description and first look on the HARPS(-N) radial velocity datasets

Northern and southern spectroscopic observations of K2-3 were carried out between January 22, 2015 and July 7, 2017, producing a total of 211 HARPS-N and 138 HARPS spectra. Of

---

[1] http://www.speculoos.ulg.ac.be/cms/c_3272698/en/speculoos-portail

the 349 spectra, 283 are unpublished observations while 66 HARPS observations were previously published by Almenara et al. (2015). The HARPS-N spectra come from two independent programmes: the HARPS-N Collaboration Guaranteed Time Observations (GTO)[2] and the Global Architecture of Planetary Systems programmes (GAPS; Benatti et al. 2016). The two collaborations shared observing time on this target to maximize the number of RV measurements and to optimize the observing strategy. The spectra were reduced with the version 3.7 of the HARPS-N Data Reduction Software (DRS; Cosentino et al. 2014). The extraction and wavelength calibration of the HARPS spectra were performed using the on-line pipeline (Lovis & Pepe 2007). The exposure time was fixed at 1800 s for both instruments, producing a typical signal-to-noise ratio $S/N = 30$ at a wavelength $\lambda \sim 550$ nm.

2.1. Definition of the final dataset

We excluded some observations from our analysis for two reasons. We did not consider spectra with a $S/N \leq 11$ as measured at $\lambda = 550$ nm (echelle orders 46 and 49 for HARPS-N and HARPS, respectively). We then identified RV measurements potentially contaminated by scattered moonlight. This is particularly important for faint targets such as K2-3, which lie close to the ecliptic plane. Using the procedure described in Sect. 2.1 of Malavolta et al. (2017), we identified five HARPS-N spectra that are probably contaminated by scattered moonlight, and we discarded them from the dataset[3]. We could not perform the same analysis on the full HARPS dataset because nearly half of those spectra were acquired with simultaneous Fabry-Perot and not with fibre B on sky. Nonetheless, we adopted a heuristic approach[4] to identify four potentially contaminated measurements, which we removed from the final dataset[5]. After these cuts, our final dataset includes 197 HARPS-N spectra and 132 HARPS spectra.

2.2. Radial velocity extraction

In this study we primarily use RVs extracted with the TERRA pipeline (Anglada-Escudé & Butler 2012). The TERRA pipeline is commonly used to extract RVs of M dwarfs because it typically provides measurements with better precision and lower scatter than those extracted for low-mass stars with the CCF recipe of the on-line DRS pipeline (Perger et al. 2017). The HARPS fibre link was upgraded with octagonal fibres on May 28, 2015 (Lo Curto et al. 2015), introducing an RV offset between data acquired before and after the upgrade. We accounted for this offset by producing *pre-* and *post-upgrade* spectral templates to extract the RVs, and by introducing a velocity zero point offset for each dataset as free parameter when fitting the time series.

The TERRA RV time series are listed in the on-line Tables A.1 and A.2 for HARPS-N and HARPS, respectively. The median values of the internal errors are 1.88 m s^{-1} for HARPS-N and 2.04 m s^{-1} for HARPS.
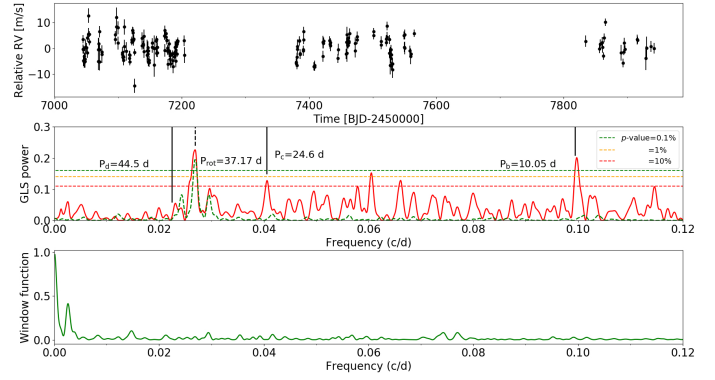
Fig. 1. *Upper plot*: time series of the K2-3 RVs extracted with the pipeline TERRA using the HARPS-N spectra. *Middle plot*: GLS periodogram of the RV time series (red line) is shown. Three levels of *p*-values are indicated by the horizontal dashed lines. The green dashed line overplotted on the RV periodogram represents the window function of the measurements (*bottom plot*) shifted in frequency to be superimposed on the strongest peak of the RV periodogram. This helps to identify the alias frequencies of the most relevant peaks. The stellar rotation and planetary orbital frequencies are indicated by vertical lines and corresponding labels.

2.3. Preliminary RV frequency analysis

We conducted a preliminary analysis of the RV datasets using the generalized Lomb-Scargle (GLS) algorithm (Zechmeister & Kürster 2009) to identify significant signals. We performed the GLS frequency analysis of the northern and southern datasets separately along with the combined RV dataset, removing RV offsets as determined by the analysis described in Sect. 4. We show the resulting periodograms in Figs. 1–3.

The HARPS-N periodogram is dominated by a signal at 37.2 ± 0.1 days[6], which we identify as the rotation period of the star (see Sect. 3). This signal has a *p*-value = 0.01%, as estimated by bootstrapping the data, i.e. by randomly drawing the RV measurements (with replacement) and generating 10 000 mock datasets. Its semi-amplitude is 2.9 ± 0.3 m s^{-1}, as estimated with GLS, slightly lower than the RMS of the data (4.1 m s^{-1}). A significant peak with a slightly lower power appears at the orbital period of K2-3 b, while the peak corresponding to the orbital period of K2-3 c appears with less significance (*p*-value $\sim$1%). The orbital period of K2-3 d is undetected in the HARPS-N periodogram.

The HARPS periodogram is dominated by the orbital period of K2-3 b (Fig. 2; *p*-value = 0.01%). The signal produced by the stellar rotation has a *p*-value around 1%, therefore it is much less significant than in the HARPS-N data. The window function is responsible for a pattern of alias frequencies around these signals. In addition to the one-year aliases, one-month aliases (synodic month frequency $f_{s.m.} = 0.03386$ c/d) are also probably present, which is expected for a star near to the ecliptic. For example, a one-month alias of the 37-day signal occurs at 0.061 c/d (=1/37+$f_{s.m.}$ c/d), while a one-month alias of P_b occurs at 0.065 c/d. Both aliases are visible in Fig. 2.

The signals that most clearly emerge in the periodogram of the combined dataset are those of the planet K2-3 b and the stellar rotation period, which are highly significant and have almost the same power (Fig. 3). The signal of planet K2-3 c is more weakly present with a *p*-value $\sim$1%.
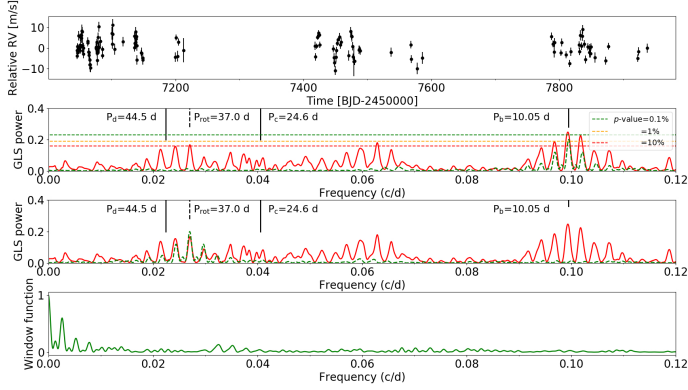
Fig. 2. As in Fig. 1 but for TERRA RVs extracted from the HARPS spectra. *Pre-* and *post-*upgrade RV offsets have been applied, as derived from our analysis described in Sect. 4.
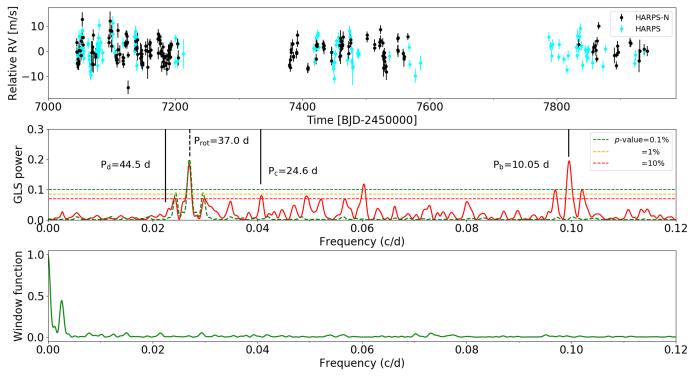

Fig. 3. As in Fig. 1 but for all TERRA HARPS-N and HARPS RVs. We applied an offset to each separate dataset, as derived from our analysis described in Sect. 4.

3. Stellar parameters and activity

The main properties of the star K2-3 are summarized in Table 1. While K2-3 has previously been characterized by Crossfield et al. (2015) and Almenara et al. (2015), we independently determined the stellar parameters from our HARPS-N spectra using the method developed by Maldonado et al. (2015)[7]. We estimated the effective temperature and iron abundance of the star using measurements of the pseudo-equivalent widths of the spectral features. We then determined stellar mass, radius, and surface gravity using empirical relationships. Our results are consistent with, but slightly more precise than, previous estimates. We adopted these new values for the analysis in the rest of the paper.

3.1. Photometry

The K2 light curve of K2-3, with all the transit signals removed, is shown in Fig. 4. We used the K2SFF[8] light curve processed as described by Vanderburg & Johnson (2014) and Vanderburg et al. (2016a). The light curve shows a quasi-periodic modulation with a flux semi-amplitude of ~0.1%. There is also clear evidence for changes from one rotation to the next, likely due to the evolution of active regions. In the bottom panel of Fig. 4 we show the GLS periodogram of the binned K2 light curve (one point

Table 1. Stellar parameters for K2-3

Parameter	Value	Ref.
RA [deg, ICRS J2015]	172.3353579	
Dec [deg, ICRS 2015]	−1.4551256	
Mass [$M_\odot$]	0.62±0.06	(1)
	0.60±0.09	(2)
	0.61±0.09	(3)
	0.60±0.09	(4)
Radius [$R_\odot$]	0.60±0.06	(1)
	0.56±0.07	(2)
	0.55±0.04	(3)
	0.56±0.07	(4)
Effective temperature, T_{eff} [K]	3835±70	(1)
	3896±189	(2)
[Fe/H]	−0.01±0.09	(1)
	−0.32±0.13	(2)
Surface gravity, $\log g$ [$\log_{10}$(cgs)]	4.66±0.05	(1)
	4.73±0.06	(3)
	4.72±0.13	(4)
Density [$\rho_\odot$]	3.51±0.61	(3)
$\log(L/L_\odot)$	−1.15±0.09	(1)
Age [Gyr]	⩾1	(2)

Notes. (1) This work: derived from HARPS-N spectra using the method described by Maldonado et al. (2015); (2) Crossfield et al. (2015); (3) Almenara et al. (2015); and (4) Sinukoff et al. (2016).

per day), which shows a strong peak at $P_{rot} = 38.3 \pm 0.7$ days[9]. Even though the K2 light curve was obtained about six months before the first spectroscopic observations and only covers about two rotation periods, the high S/N photometry is useful for constraining the stellar rotation period. It is interesting to note that, while the amplitude of the photometric rotational variability of the star is fairly low, the stellar rotation frequency is nonetheless the strongest signal in the RV time series of the star.

We also obtained time-series photometry of K2-3 from the MEarth survey (Irwin et al. 2015). We monitored K2-3 with one of the 40 cm telescopes of the Southern MEarth array from January 21, 2015 to April 4, 2016. With a total of 8669 data points, the light curve overlaps with the first two seasons of the spectroscopic observations. The fact that the MEarth data are contemporaneous with many of our RV observations and their high photometric precision (due in part to the excellent observing conditions at Cerro Tololo), make the MEarth light curve potentially useful for characterizing the stellar activity. We analysed the MEarth data (in nightly bins) by calculating a GLS periodogram. The highest peak in the periodogram is at 31.8 ± 0.2 days with a semi-amplitude of ~1 mmag (Fig. 5). This period does not correspond to the more robust stellar rotation period derived from the uninterrupted observations of K2 or using the H_α spectroscopic indicator (Sect. 3.2); nonetheless the result is worth mentioning because the data have been collected with uneven sampling by a ground-based small-aperture telescope and they show very low amplitude modulation compared to the typical photometric error. The periodogram also shows an additional peak at a period of about ~230 days, without any counterpart in the window function. While the signal could be due to systematics present in the MEarth data, its nature
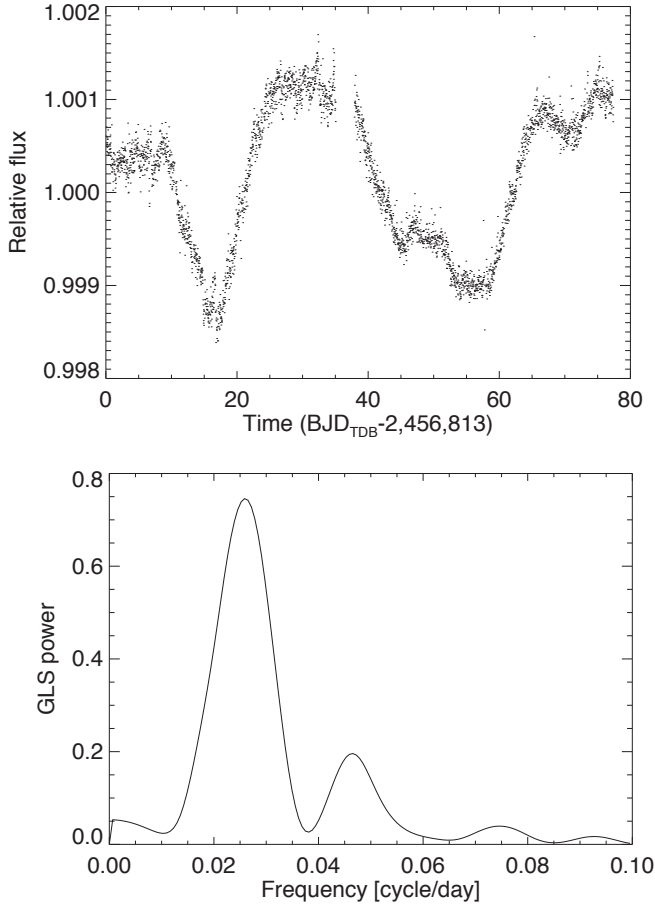
Fig. 4. *Top plot*: K2 light curve of K2-3 with the planetary transits removed. *Bottom plot*: GLS periodogram of the binned light curve (one point per day), showing a peak at $P_{rot} = 38.3$ days.

is unclear and an astrophysical origin cannot be ruled out (see Sect. 3.2).

3.2. Spectroscopic activity indexes

We studied the activity level of K2-3 during the time period of our observations using the Hα line as a spectroscopic activity indicator, which we extracted from our spectra using the method described by Gomes da Silva et al. (2011)[10]. The time series of the Hα activity indicator is shown in Fig. 6 and the data are listed in Table A.5. We analysed the time series by calculating a GLS periodogram to identify periodicities related to a possible activity cycle and stellar rotation. The GLS periodogram is shown in the second and third panels of Fig. 6.

The highest peak in the periodogram occurs at $P = 211 \pm 3$ days, and has a power comparable to that of its one-year alias frequency at ~450 days. The existence of a long-term modulation is especially clear after looking at the data of the first two seasons. A bootstrap (with replacement) Monte Carlo analysis based on 10 000 mock datasets reveals that these peaks are statistically significant and have false alarm probabilities lower than 0.1%. We are, however, unable to ascertain whether the 211-day period or its alias at 450 days is the true underlying period. The origin of this long-period signal is unclear. If the signal is astrophysical, one possible

---

[10] We did not analyse the activity indicator based on the CaII H&K lines because of the very low S/N in this spectral region.
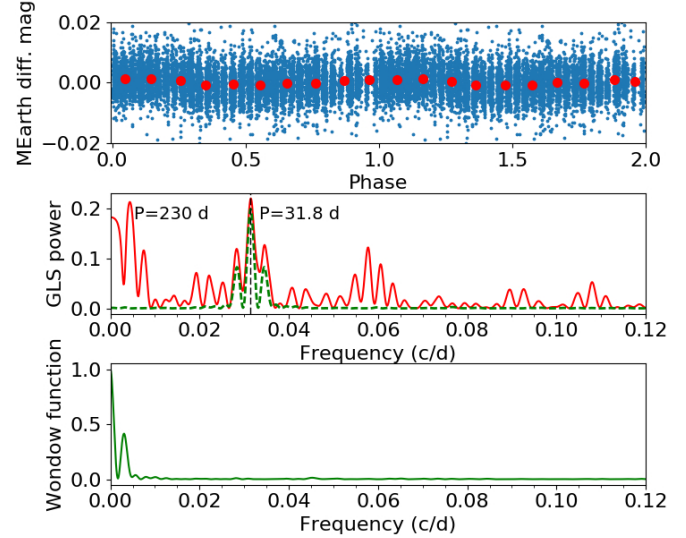

Fig. 5. *Top plot*: light curve of K2-3 from the MEarth-south survey, folded at the best period $P = 31.8$ days found using GLS. *Middle plot*: GLS periodogram of the MEarth light curve. The green line corresponds to the window function of the measurements (*bottom plot*), which is shifted in frequency so that the peak is superimposed on the major peak of the RV periodogram to directly identify alias frequencies.

explanation is an intermediate-duration activity cycle. Some tentative evidence exists for such cycles in low-mass stars (Savanov 2012; Robertson et al. 2013) and could represent sub-cycles superimposed on longer duration activity cycles, as observed for the Sun (so-called Rieger cycles). We note that the 211-day period is close to the 230-day signal observed in the MEarth photometry.

The second highest peak in the periodogram of the Hα indicator is close to the expected stellar rotation period and is highly significant ($P = 40.3 \pm 0.1$ days, p-value < 0.1%). This signal is particularly strong in the last season of observations; during this time, a clear modulation related to P_{rot} is visible in the Hα time series, which covers nearly four stellar rotations. A GLS analysis of only the last season of observations identifies a periodicity of 43.5 ± 1.0 days. Folding the data at this period reveals that the modulation does not have a simple sinusoidal shape (Fig. 7).

4. Gaussian process regression analysis of radial velocities

We used the stellar activity information derived in Sect. 3 to perform a detailed analysis of the combined HARPS-N and HARPS RV datasets within a Bayesian framework based on GP regression. It has now become standard in RV analysis to use GPs to model the stellar contribution to the RV variations jointly with a number of Keplerian functions describing the planetary orbital motion (see Haywood et al. 2014 for the first application of this technique). This approach has proven to be a powerful to retrieve planetary masses from high-precision RV measurements when a signal closely related to the stellar rotation period, or its harmonics, is present in the RV time series (Dumusque et al. 2017).

For a general description of the GP method, and its performance when applied to RV time series, we refer, amongst others, to the recent works by López-Morales et al. (2016), Cloutier et al. (2017), Damasso & Del Sordo (2017), and Dittmann et al. (2017). The GP regression is based on the choice
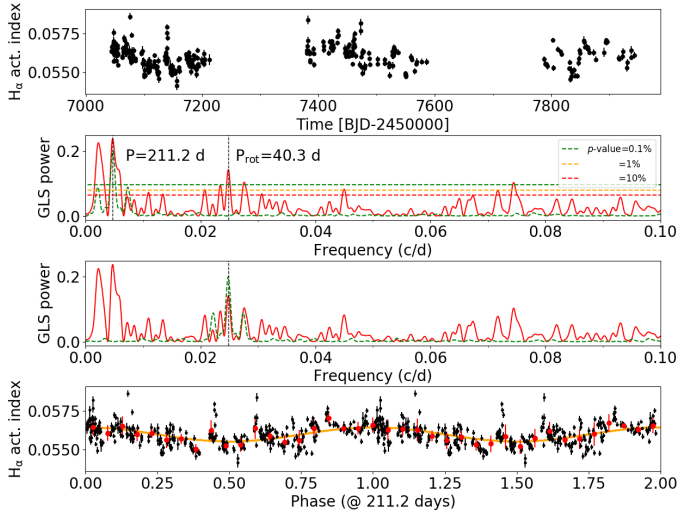
Fig. 6. *Top plot*: time series of the activity indicator based on the Hα line extracted from the HARPS and HARPS-N spectra. *Second and third plots*: GLS periodogram of the dataset is shown. The dashed horizontal lines indicate the p-value levels as derived from a bootstrap analysis. The green curve corresponds to the window function of the measurements, which is shifted in frequency so that the peak is superimposed on the major peak of the RV periodogram (*second plot*), to directly identify alias frequencies. In the *third plot* the window function is shifted to be superimposed on the P ~ 40 days rotational signal. *Bottom*: time series phase-folded at the period P = 211 days. Red points represent the average of the data within 20 bins in the phase range [0,1].

of a specific kernel; i.e. a covariance matrix describing the correlation between measurements taken at two different epochs. For the case of K2-3, the so-called *quasi-periodic* (q-p) kernel is particularly useful because a signal very likely related to the stellar rotation period P_{rot} dominates the RV time series (Sect. 2), and there is evidence for an evolutionary timescale of the active regions close to P_{rot} (Sects. 3.1 and 3.2). Each element of the covariance matrix has the form

$$K(t, t') = h^2 \cdot \exp\left[-\frac{(t-t')^2}{2\lambda^2} - \frac{sin^2(\frac{\pi(t-t')}{\theta})}{2w^2} \right]$$
$$+ \left[\sigma_{RV,instr}^2(t) + \sigma_{jit,instr}^2 \right] \cdot \delta_{t,t'}, \quad (1)$$

where t and t' represent two different epochs. The first term represents the quasi-periodic kernel, which is composed of a periodic term and an exponential decay term. This functional form is suitable for modelling a recurrent signal linked to stellar rotation and takes into account the finite lifetime of the active regions. Eq. (1) contains four covariance matrix hyperparameters: h represents the amplitude of the correlations; θ represents the rotation period of the star; w is the length scale of the periodic component, linked to the size evolution of the active regions; and λ is the correlation decay timescale, which can be physically related to the active regions lifetime. The remaining parameters in Eq. (1) are $\sigma_{RV,instr}(t)$, which is the RV internal error at time t for each spectrograph (or independent dataset); $\sigma_{jit,instr}$, which are additional uncorrelated jitter terms, one for each instrument (or independent dataset), which we add in quadrature to the internal errors to account for additional instrumental effects and noise sources neither included in $\sigma_{RV,instr}(t)$ nor modelled by the q-p kernel; and $\delta_{t,t'}$, which is the Kronecker delta function.

Our GP analysis was based on a Markov chain Monte Carlo (MCMC) algorithm. The model, algorithms, and statistical
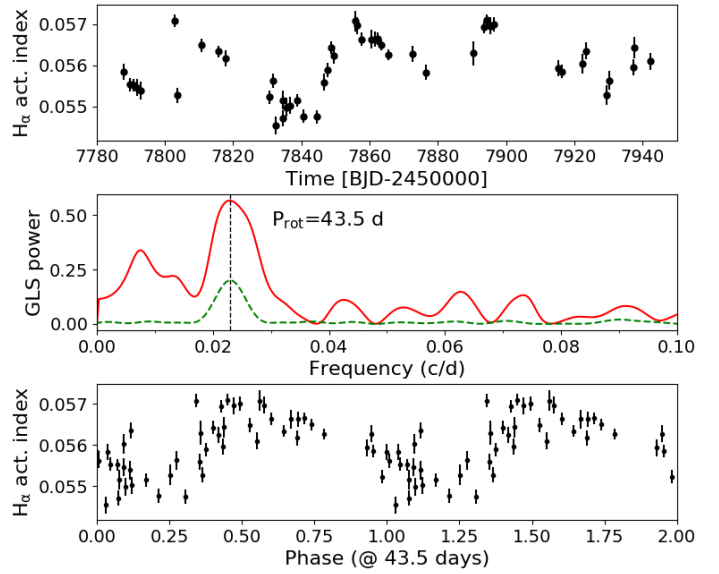
Fig. 7. *Top plot*: time series of the activity indicator based on the Hα line extracted from the HARPS and HARPS-N spectra. Here, only the dataset of the third season is shown. *Middle plot*: GLS periodogram of the dataset is shown. The green line corresponds to the window function of the measurements, which is shifted in frequency so that the peak superimposes to the major peak of the RV periodogram, to directly identify possible alias frequencies. *Bottom plot*: time series phase-folded at the period P = 43.5 days.

framework used in this work are the same as described in Damasso & Del Sordo (2017), and we refer to that work for a detailed description. In this work, we assumed circular orbits for all the planets. The best-fit values and uncertainties for each jump parameter were calculated as the median of the marginal posterior distributions and the 16% and 84% quantiles.

4.1. Choice of the priors

The priors adopted in our analysis are listed in Table 2. In this subsection, we describe and justify some of our choices for the priors.

In our fits, we allowed the semi-amplitude h of the correlated stellar signal to vary up to a value of 5 m s^{-1}, which represents nearly twice the value estimated by GLS at $P = 37$ days. The prior range used for the stellar rotation hyperparameter θ is defined based on our rotation period estimates from the K2 photometry and Hα activity indicator. This also takes into account the results of a trial MCMC analysis that was run after the conclusion of the second observing season, which adopted a larger prior range and indicated that the posterior distribution was well constrained within the range [35, 43] days.

For the active regions evolutionary timescale λ we adopted a uniform prior between 20 and 60 days, corresponding nearly to $P_{rot}/2$ and $1.5 \cdot P_{rot}$. This choice was first motivated by the marginal posterior obtained with the trial MCMC analysis of the dataset for the first and second seasons, which is symmetric around $\lambda = 36$ days ($\sigma \sim 8$ days). An evolutionary timescale of the order of the stellar rotation period could also be guessed directly by looking at the K2 light curve, which shows changes in its pattern from one rotation to the next[11]. We also used the results of Giles et al. (2017; Eq. (8)) to get a loose estimate

---

[11] Due to the short time baseline, we could not constrain λ through the analysis of the autocorrelation function, as done by López-Morales et al. (2016) using the longer baseline of the *Kepler* photometry.

of the timescale based on the RMS of the K2 data and the stellar effective temperature. The equation for determining the timescale was derived by Giles et al. (2017) using a calibration sample not biased by spectral type and, although faster rotators than K2-3 were analysed in the Giles et al. work, this result could be tentatively used for a star with $P_{\rm rot} = 40$ days. With an $RMS = 7.6 \times 10^{-4}$ mag and $T_{\rm eff} = 3835$ K, we get a timescale of 38^{+19}_{-13} days.

For the planetary orbital parameters, we fixed the upper limit of the Keplerian semi-amplitude to 5 m s^{-1} for K2-3 b and K2-3 c, and to 3 m s^{-1} for planet K2-3 d. For K2-3 b, $K = 5$ m s^{-1} is more than twice the value estimated by GLS after removing the stellar rotation signal, and represents a conservative upper limit also for the planet K2-3 c. For the outermost planet, K2-3 d, the absence of a signal in the GLS periodogram suggests that $K_{\rm d}$ should be significantly lower. The priors on the orbital period and time of transit were taken from Beichman et al. (2016), who determined the ephemerides by combining K2 observations with additional transits observed with the *Spitzer* space telescope.

4.2. Analysis of the combined radial velocity dataset

We analysed the full RV dataset without binning the data when more than one observation is available during the same night. To guarantee a wide exploration of the parameter space, we adopted 150 independent chains properly initialized to start from well separated locations. We discarded the first 3 000 steps of each chain by resetting the sampler. The MCMC chains reached the convergence according to the Gelman-Rubin statistics after 18 000 steps, and a further burn-in (0.75% of the total steps) was applied to calculate the best-fit values of the parameters (see Eastman et al. 2013 and references therein).

We show the best-fit results for all the free parameters and derived quantities in Table 3. The mass of the super-Earth K2-3 b is robustly determined with a S/N of ∼7σ, while the mass of K2-3 c is detected with a lower significance of 2.6σ. The mass of K2-3 d remains undetermined, with a 1σ upper limit of about ∼2$M_\oplus$. This suggests that the mass of K2-3 d is too low to be detected, but it is also plausible that the low amplitude of the Doppler signal, compared to that of the stellar activity component, and its proximity to the stellar rotation period allow the signal to be absorbed into our GP activity model (Vanderburg et al. 2016b). We investigate the robustness of this upper limit in Sects. 5.1 and 5.2.

We show the RV curves in Fig. 8, with the stellar activity contribution subtracted, and folded at the best-fit orbital periods. The stellar contribution to the RV time series resulting from our fit is shown in Fig. 9. The stellar activity component of the model is reliably described by our best-fit results. The stellar rotation period and the evolutionary time scale of the active regions appear to be well characterized for both datasets. As we have found from the analysis of the RV datasets of other targets, the GP quasi-periodic regression tends to suppress low frequencies in the residuals. This means that if an additional long-term modulation is actually present in the original data, and it is not explicitly included in the fitted model, it would be absorbed by the stellar activity component and disappear in the residuals, after removing the planetary solutions. However, we note that the data in Fig. 9 do not show any long-term trend residual suggestive of an activity cycle or a longer period companion to K2-3 not included in our global model. We also note that the stellar rotation period, as retrieved by the GP regression, differs from that derived with GLS by ∼3 days. This difference

Table 2. Prior probability distributions for the three-planet circular model parameters.

Jump parameter	Prior
h [m s^{-1}]	$\mathcal{U}\,(0.5, 5)$
λ [days]	$\mathcal{U}\,(20, 60)$
w	$\mathcal{U}\,(0.001, 1)$
θ [days]	$\mathcal{U}\,(35, 43)$
$K_{\rm b}$ [m s^{-1}]	$\mathcal{U}\,(0.05, 5)$
$P_{\rm b}$ [days]	$\mathcal{N}\,(10.054544, 0.000029^2)$ [a]
$T_{0,\rm b}$ [BJD-2 400 000]	$\mathcal{N}\,(56813.42024, 0.00094^2)$ [a]
$K_{\rm c}$ [m s^{-1}]	$\mathcal{U}\,(0.05, 5)$
$P_{\rm c}$ [days]	$\mathcal{N}\,(24.64638, 0.00018^2)$ [a]
$T_{0,\rm c}$ [JD-2 400 000]	$\mathcal{N}\,(56812.2777, 0.0026^2)$ [a]
$K_{\rm d}$ [m s^{-1}]	$\mathcal{U}\,(0.05, 3)$
$P_{\rm d}$ [days]	$\mathcal{N}\,(44.55765, 0.00043^2)$ [a]
$T_{0,\rm d}$ [JD-2 400 000]	$\mathcal{N}\,(56826.2248, 0.0038^2)$ [a]
$\gamma_{\rm HARPS-N}$ [m s^{-1}]	$\mathcal{U}\,(-10, +10)$
$\gamma_{\rm HARPS-pre}$ [m s^{-1}]	$\mathcal{U}\,(-10, +10)$
$\gamma_{\rm HARPS-post}$ [m s^{-1}]	$\mathcal{U}\,(-10, +10)$
$\sigma_{\rm jit,HARPS-N}$ [m s^{-1}]	$\mathcal{U}\,(0.05, 5)$
$\sigma_{\rm jit,HARPS-pre}$ [m s^{-1}]	$\mathcal{U}\,(0.05, 5)$
$\sigma_{\rm jit,HARPS-post}$ [m s^{-1}]	$\mathcal{U}\,(0.05, 5)$

Notes. [a] Ephemeris from Beichman et al. (2016), derived from transit observations with K2 and *Spitzer*. T_0 is the time of inferior conjunction.

is because the functional form of the quasi-periodic kernel used to model the stellar contribution is different from the simple sinusoid used by the GLS periodogram. We calculated the GLS periodogram of the GP quasi-periodic stellar activity timeseries and found the strongest peak at $P = 37$ days, reproducing the period found in our GLS analysis of the RV dataset. The RMS of the residuals is 2.6 m s^{-1}, only slightly higher than the median of the internal errors.

4.3. Cross-check with the alternative RV extraction method

In order to test the robustness of the results using RVs obtained with the TERRA dataset, we also extracted the RVs using an independent pipeline described by Astudillo-Defru et al. (2015, 2017). In brief, this pipeline works by aligning all the spectra to a common reference frame by removing the Earth's barycentric RV and by using the RVs of K2-3 measured by the DRS as an initial guess. Then a median template is computed from the aligned spectra and regions of the spectra contaminated by tellurics are rejected. The template is used to calculate a chi-square profile as a function of RVs for each individual spectrum, whose minimum corresponds to the stellar RV.

The RVs from this alternative pipeline are listed in Tables A.3, A.4. We performed the same analysis as described in Sect. 4.2 with the data from this alternative pipeline, and found that the results of this analysis (shown in Table 3) are in very good agreement with those obtained with TERRA. In particular, the planetary parameters are all in agreement within 1σ, strengthening our findings.

5. Assessing the reliability of the derived planetary masses

The results of the analysis presented in Table 3 show that while the Doppler signal of the innermost planet is retrieved with a

Table 3. Best-fit solutions for the quasi-periodic GP model applied to the combined HARPS/HARPS-N RV time series extracted with TERRA and an alternative pipeline.

Jump parameter	Best-fit value	
	TERRA	alternative pipeline
Stellar activity GP model		
h [m s^{-1}]	$2.9^{+0.4}_{-0.3}$	$3.1^{+0.5}_{-0.3}$
λ [days]	$40.0^{+10.4}_{-9.0}$	$43.5^{+9.8}_{-8.9}$
w	$0.18^{+0.11}_{-0.04}$	0.26 ± 0.07
θ [days]	$40.4^{+1.1}_{-1.9}$	$39.8^{+1.1}_{-0.9}$
Uncorrelated jitter		
$\sigma_{\text{jit,HARPS-N}}$ [m s^{-1}]	1.4 ± 0.3	0.6 ± 0.4
$\sigma_{\text{jit,HARPS-pre}}$ [m s^{-1}]	2.2 ± 0.5	2.5 ± 0.5
$\sigma_{\text{jit,HARPS-post}}$ [m s^{-1}]	2.0 ± 0.6	1.6 ± 0.6
RV offset		
$\gamma_{\text{HARPS-N}}$ [m s^{-1}]	$-0.06^{+0.54}_{-0.57}$	$30149.2^{+0.6}_{-0.7}$
$\gamma_{\text{HARPS-pre}}$ [m s^{-1}]	$0.20^{+0.75}_{-0.79}$	$30480.2^{+0.8}_{-0.9}$
$\gamma_{\text{HARPS-post}}$ [m s^{-1}]	$0.002^{+0.670}_{-0.688}$	30479.2 ± 0.8
Planetary orbital parameters		
K_{b} [m s^{-1}]	2.7 ± 0.4	2.9 ± 0.4
P_{b} [days]	10.05454 ± 0.00003	10.05454 ± 0.00003
$T_{0,\text{b}}$ [BJD-24 00 000]	56813.42022 ± 0.00095	56813.42025 ± 0.00095
K_{c} [m s^{-1}]	0.95 ± 0.37	0.98 ± 0.34
P_{c} [days]	24.64638 ± 0.00017	24.64638 ± 0.00018
$T_{0,\text{c}}$ [BJD-24 00 000]	56812.2777 ± 0.0026	56812.2778 ± 0.0026
K_{d} [m s^{-1}]	$0.29^{+0.34}_{-0.18}$ [<0.43 (68.3th perc.)]	$0.31^{+0.35}_{-0.20}$ [<0.47 (68.3th perc.)]
P_{d} [days]	44.55764 ± 0.00042	44.55766 ± 0.00043
$T_{0,\text{d}}$ [BJD-24 00 000]	56826.2248 ± 0.0037	56826.2247 ± 0.0038
Planetary radii [a]		
$R_{\text{p,b}}$ ($R_\oplus$)	2.29 ± 0.23	
$R_{\text{p,c}}$ ($R_\oplus$)	1.77 ± 0.18	
$R_{\text{p,d}}$ ($R_\oplus$)	1.65 ± 0.17	
Quantities derived from RVs [b]		
$M_{\text{p,b}}$ ($M_\oplus$)	6.6 ± 1.1	7.0 ± 1.0
$M_{\text{p,c}}$ ($M_\oplus$)	$3.1^{+1.3}_{-1.2}$	$3.2^{+1.2}_{-1.1}$
$M_{\text{p,d}}$ ($M_\oplus$)	$1.2^{+1.4}_{-0.7}$ [<1.8 (68.3th perc.)]	$1.3^{+1.5}_{-0.8}$ [<1.9 (68.3th perc.)]
	$2.7^{+1.2}_{-0.8}$ (see Sect. 5.1)	
$\rho_{\text{p,b}}$ [g cm^{-3}]	$3.0^{+1.3}_{-0.9}$	$3.2^{+1.3}_{-0.9}$
$\rho_{\text{p,c}}$ [g cm^{-3}]	$3.1^{+1.9}_{-1.3}$	$3.2^{+1.8}_{-1.3}$
$\rho_{\text{p,d}}$ [g cm^{-3}]	$1.6^{+2.1}_{-1.0}$ [<2.4 (68.3th perc.)]	$1.6^{+2.1}_{-1.0}$
	$3.1^{+2.0}_{-1.2}$ (see Sect. 5.1)	
$a_{\text{p,b}}$ [AU]	$0.0777^{+0.0024}_{-0.0026}$	
$a_{\text{p,c}}$ [AU]	$0.1413^{+0.0044}_{-0.0047}$	
$a_{\text{p,d}}$ [AU]	$0.2097^{+0.0065}_{-0.0070}$	

Notes. Our global model includes three orbital equations (circular case). [a]Radii are derived using our estimate for the stellar radius, R = 0.60 ± 0.06 $R_\odot$, and the ratios $R_{\text{planet}}/R_{\text{star}}$ derived by Beichman et al. (2016) from K2 and *Spitzer* data. [b]Derived quantities from the posterior distributions. We used the following equations (assuming $M_{\text{s}} + m_{\text{p}} \cong M_{\text{s}}$): $m_{\text{p}}\sin i \cong (K_{\text{p}} \cdot M_{\text{s}}^{\frac{2}{3}} \cdot \sqrt{1 - e^2} \cdot P_{\text{p}}^{\frac{1}{3}})/(2\pi G)^{\frac{1}{3}}$; $a \cong [(M_{\text{s}} \cdot G)^{\frac{1}{3}} \cdot P_{\text{p}}^{\frac{2}{3}}]/(2\pi)^{\frac{2}{3}}$, where G is the gravitational constant.